Michael Matson
NOAA National Earth Satellite Service
Washington, DC 20233
Jeff Dozier
Department of Geography
University of California
Santa Barbara, CA 93106

Identification of Subresolution High Temperature Sources Using a Thermal IR Sensor

Steel mills, and gas flares from oil fields, were identified by using the 3.8-μm and 11-μm sensors on board the NOAA-6 satellite.

Introduction

The third-generation, polar orbiting, TIROS-N series of environmental satellites provides two thermal infrared (IR) channels for twice-daily monitoring of the Earth's surface (see Table 1). Part of the four-channel Advanced Very High Resolution Radiometer (AVHRR), the 3.8 μm thermal IR channel, was designed to supplement the 11-μm thermal IR channel in the computation of sea surface temperature by providing corrections for atmospheric water vapor and cloud contamination. The best spatial resolution for the two thermal channels is 1.1 km at the satellite subpoint, and the minimum noise-equivalent differential temperature (NEΔT) is 0.12 K for 300-K scene (Schwalb, 1979). Calibration is provided on board for converting the satellite-measured thermal energy emitted by the Earth and its atmosphere into brightness temperatures. Unless these temperatures are corrected for land-surface emissivity, as well as for absorption and re-emission in the intervening atmosphere, they cannot be compared strictly with Earth surface thermodynamic temperatures.

Although designed for sea surface temperature studies, initial examination of the 3.8-μm data over land areas revealed differences between them and the 11-μm data. Specifically, as shown by the computer-enhanced NOAA-6 satellite image of the midwestern United States in Figure 1, the 3.8-μm data accentuate high temperature areas (Table 2). These areas are not as apparent in the 11-μm data, as is readily revealed by a brightness temperature plot across a high temperature area (Figure 1, number 5) in Cleveland, Ohio (see Figure 2). At this high radiation source the 3.8-μm brightness temperature is 34.5 K higher than the 11-μm brightness temperature. A typical brightness temperature difference between the two channels, 1 to 1.5 K, is shown by the rest of the plot and is caused primarily by less water vapor attenuation in the 3.8-μm channel (Weinreb and Hill, 1980). The purposes of this paper are to (1) present the radiance-temperature relations that explain the different responses of the two thermal-IR channels to a common target; (2) demonstrate how the different responses of the two channels can be used to determine both the brightness temperature of the source causing the two-channel difference and the area of the pixel (picture element) covered by

Abstract: *Simultaneous use of the 3.8-μm and 11-μm thermal infrared channels on board the 3rd-generation NOAA-6 environmental satellite provides the capability to detect subresolution scale high-temperature sources, and to estimate both the temperature and size of such sources. Examples presented include gas flares from oil fields in the Middle East and steel mills in the midwestern United States.*

Photogrammetric Engineering and Remote Sensing,
Vol. 47, No. 9, September 1981, pp. 1311-1318.

0099-1112/81/4709-1311$02.25/0

TABLE 1. NOAA-6 AVHRR SPECTRAL CHANNELS

Channel	Spectral Interval
1	0.55–0.68 μm
2	0.725–1.10 μm
3	3.55–3.93 μm
4	10.5–11.5 μm

the source; and (3) identify the physical sources responsible for the high temperature response in the 3.8-μm channel.

RADIANCE-TEMPERATURE RELATIONS

NOTATION

c_1	first Planck constant (3.741832×10^{-16} W m^2)
c_2	second Planck constant (1.43876×10^{-2} m K)
$L_j(T)$	upwelling thermal radiance (W m^{-2} μm^{-1} sr^{-1}) in channel j as a function of thermodynamic temperature
p	portion of pixel covered by target
T	thermodynamic temperature (K)
T_j	brightness temperature (K) corresponding to radiance in channel j
T_b	blackbody temperature (K) of background
T_t	blackbody temperature (K) of target
ϵ	emissivity
λ	wavelength (μm or m)
$Y_j(\lambda)$	spectral response function of sensor in channel j

In the absence of an atmospheric contribution or attenuation, the upwelling radiance sense by a downward-pointing radiometer in channel j is derived by integrating the product of Planck's function (Suits, 1975) and the response function of the sensor, i.e.,

$$L_j(T) = \frac{10^{-6}}{\pi} \frac{\int_0^\infty \epsilon_\lambda \dfrac{c_1 \lambda^{-5}}{\exp[c_2/(\lambda T)] - 1} Y_j(\lambda)\, d\lambda}{\int_0^\infty Y_j(\lambda)\, d\lambda}$$

Here the SI units form of the Planck equation is used, so λ must be in metres. The factor 10^{-6} converts the radiance units from W m^{-3} sr^{-1} to W m^{-2} μm^{-1} sr^{-1}. For most Earth materials we ignore variations of ϵ with λ over the wavelength range of a sensor channel, and we also usually ignore variations of ϵ with sensor nadir angle. The relative response function of a sensor channel $Y_j(\lambda)$ is zero

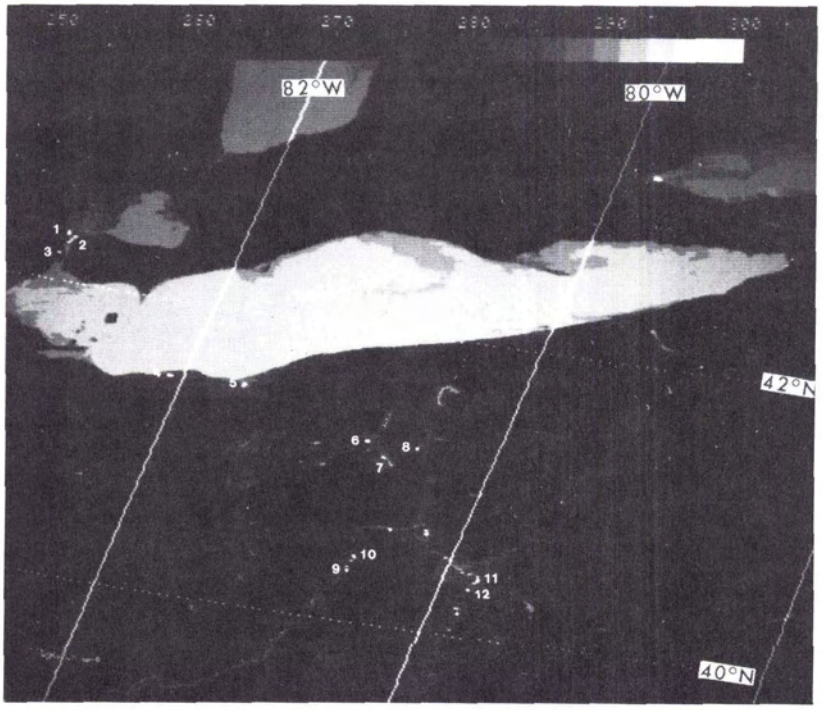

FIG. 1. NOAA-6 3.8-μm image of the midwestern United States taken on 24 September 1979 at 0015 GMT. The high temperature areas appear white and are identified in Table 2. Imagery processed by NASA/GSFC, Code 942.

TABLE 2. IDENTIFICATION OF HIGH TEMPERATURE AREAS IN THE MIDWESTERN UNITED STATES AS DETECTED BY THE NOAA-6 SATELLITE ON 24 SEPTEMBER 1979 (FIGURE 1)

Area (from Fig. 1)	High Temperature Source[1]
1	Ford Motor Company River Rouge Plant, Detroit, Michigan
2	Great Lakes Steel Company and other steel plants, Detroit, Michigan
3	McLouth Steel Corporation, Detroit, Michigan
4	U.S. Steel, Lorain, Ohio
5	Republic Steel, Cleveland, Ohio U.S. Steel, Cleveland Ohio
6	Copperweld Steel, Warren, Ohio Republic Steel, Warren, Ohio
7	U.S. Steel, Youngstown, Ohio Jones and Laughlin Steel, Youngstown, Ohio Campbell Works, Youngstown, Ohio Brierworks, Youngstown, Ohio
8	Sharon Steel, Sharon, Ohio
9	Wheeling Pitt Steel, Steubenville, Ohio
10	National Steel, Weirton, Ohio
11	U.S. Steel, Pittsburgh, Pennsylvania
12	U.S. Steel, Clairton, Pennsylvania

[1] Steel company locations provided by the U.S. Environmental Protection Agency.

outside some wavelength range (λ_1,λ_2). Within the range it is generally defined as a graphical or tabulated function, as Figure 3 shows for the 3.8 and 11 μm channels of the NOAA-6 AVHRR.

Let us designate $L_3(T)$ and $L_4(T)$ to be the NOAA-6 channel 3 (3.8 μm) and channel 4 (11 μm) radiances as functions of blackbody temperature (i.e., $\epsilon = 1$), and the inverse functions (brightness temperatures) by T_3 and T_4, respectively. Figure 4 shows conceptually the much larger increase in integrated radiance for a given increase in temperature, for channel 3 as compared to channel 4. This is because $\partial L_\lambda/\partial T$ is much greater for all wavelengths in the range 3 to 5 μm than for the range 10 to 12 μm, as can be easily demonstrated with a hand calculator (Lloyd, 1975). Figure 5 shows values of $L_3(T)$ and $L_4(T)$; these were calculated by numerically integrating Planck's equation.

DETERMINATION OF TARGET TEMPERATURES AND SIZES IN A "MIXED PIXEL"

Now, suppose we have a "mixed pixel" composed of a target blackbody temperature T_t, which occupies portion p of the pixel (where $0 \leq p \leq 1$), and a background blackbody temperature T_b, which occupies the remaining portion (1-p) of the pixel. The equations for the AVHRR brightness temperatures in channels 3 and 4 will be, in the absence of an atmospheric contribution or attenuation,

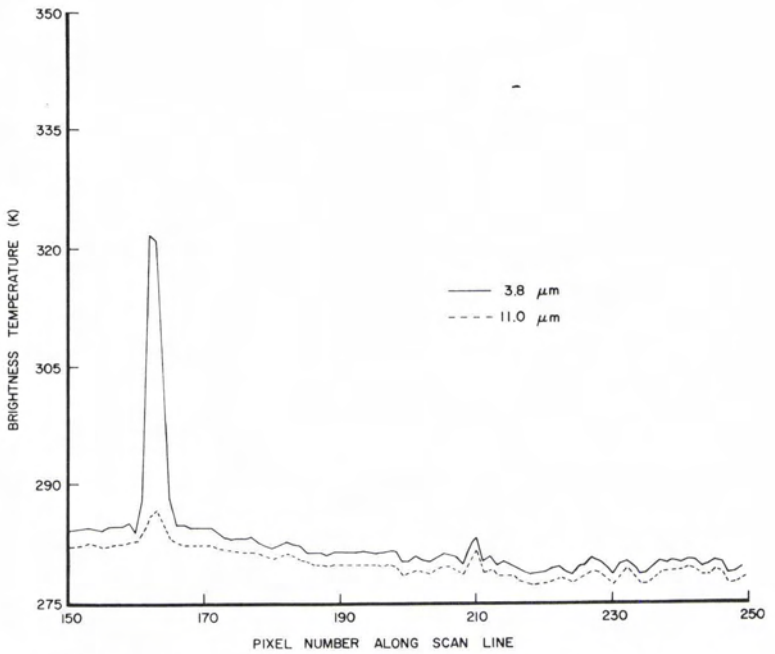

FIG. 2. 3.8-μm and 11-μm brightness temperature plot of the high temperature area in Cleveland, Ohio.

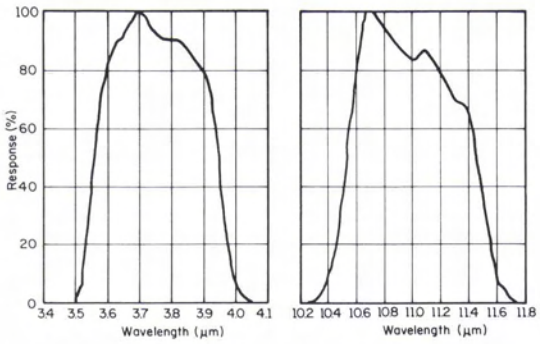

FIG. 3. Response functions (normalized to maximum values) for the 3.8-μm (left) and 11-μm (right) channels of the NOAA-6 AVHRR (from Kidwell, 1979).

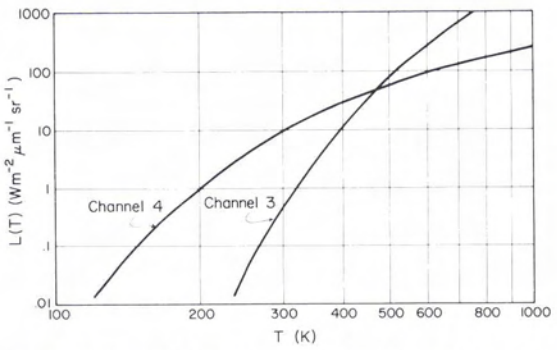

FIG. 5. Integrated Planck radiances for 3.8-μm and 11-μm channels of the NOAA-6 AVHRR, as calculated by integrating Planck's equation over the response functions of the sensors.

$$L_3(T_3) = p\, L_3(T_t) + (1 - p)\, L_3(T_b)$$
$$L_4(T_4) = p\, L_4(T_t) + (1 - p)\, L_4(T_b)$$

Dozier (1981) has shown how these equations can be solved for T_t and p, if T_b is known.

An example is presented in Figure 6. Suppose T_b = 285 K, T_3 = 325 K, and T_4 = 307 K. In Figure 6 we graph the difference T_3-T_4 as a function of p for a range of values of T_t. The dashed line represents the constraint on the solution for T_3 = 325 K. For T_3-T_4 = 18 K, the circle represents the solution p = 0.2 and T_t = 371 K. This value is a blackbody temperature. It would have to be corrected for variations in emissivity to calculate its thermodynamic temperature, but this would require that we know what material composes the target.

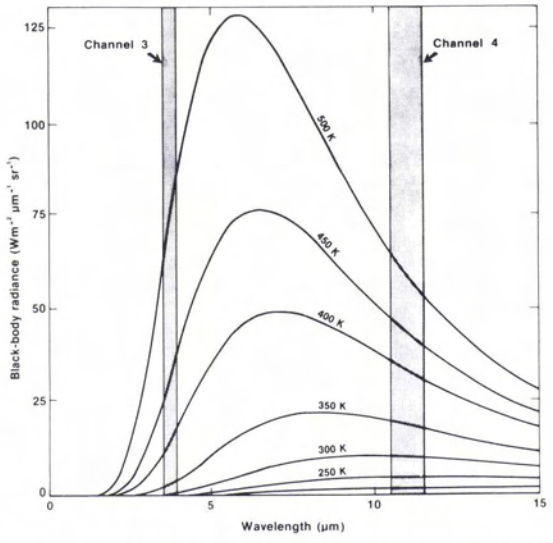

FIG. 4. Planck radiances for temperatures from 200 K to 500 K. For a given increase in temperature, the increase in area under the channel 3 segments of the curves is much greater than under the channel 4 segments.

It should be noted here that a hot target causes an increase in both T_3 and T_4, in comparison to the background area, but the increase in T_3 is much larger. A high value of T_3 that is not accompanied by at least a slight increase in the value of T_4 should therefore be interpreted as noise.

IDENTIFICATION OF HIGH TEMPERATURE SOURCES

Using the methods described in the previous section, we can examine the NOAA-6 nighttime image of the midwestern United States and quantitatively analyze the high temperature sources. A nighttime AVHRR image was used because of the danger of contamination of the 3.8-μm data by reflected solar radiation (this is not a problem in the 11-μm data). Detroit, Michigan was selected for analysis because several high temperature sources are visible within its confines. Computer-enhanced enlargements of the area are shown for the 11-μm and 3.8-μm channels in Figures 7a and 7b,

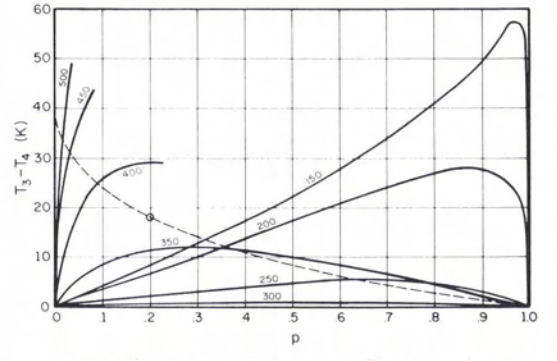

FIG. 6. Brightness temperature differences between 3.8-μm and 11-μm channels, for blackbody target temperatures from 150 to 500 K. Background blackbody temperatue is 285 K. The dashed line represents the constraint imposed by a maximum 3.8-μm brightness temperature of 325 K.

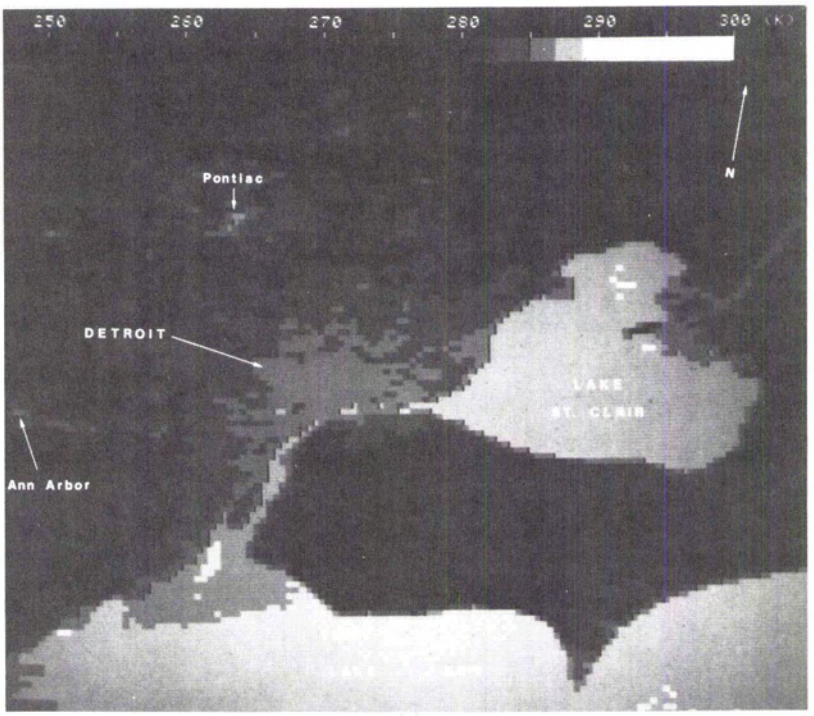

(a)

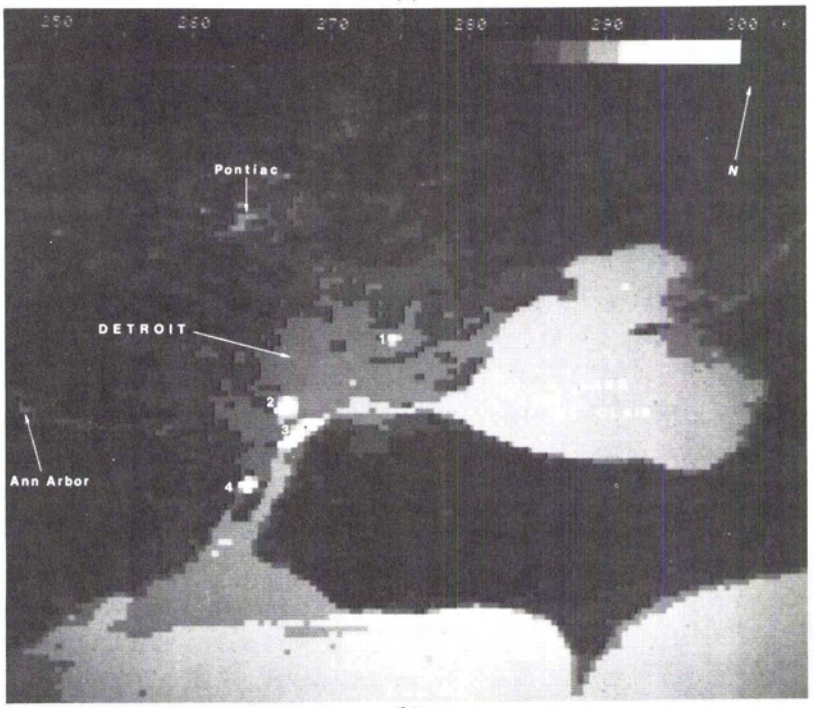

(b)

FIG. 7. (a) NOAA-6 11-μm image of the Detroit, Michigan metropolitan area taken on 24 September 1979 at 0015 GMT. Warmer areas appear gray, cooler areas black. Imagery processed by NASA/GSFC, Code 942. (b) NOAA-6 3.8-μm image of the Detroit, Michigan metropolitan area taken on 24 September 1979 at 0015 GMT. The temperature table is the same as in Figure 7a. High temperature areas 1 through 4 appear white and are identified in the text. Imagery processed by NASA/GSFC, Code 942.

respectively. The urban areas of Detroit, Pontiac, and Ann Arbor are evident in both thermal images; the use of satellite thermal imagery to detect heat islands has been well documented (Carlson *et al.*, 1977; Matson *et al.*, 1978; Price, 1979; Matson and Legeckis, 1980; Pease *et al.*, 1980). It is apparent from a comparison of Figures 7a and 7b, however, that in the 3.8-μm image there are several higher temperature areas within Detroit that are not seen on the 11-μm image. These are labeled 1 through 4 on Figure 7b. Comparison with a city map of Detroit and with Environmental Protection Agency (EPA) data show these high temperature areas to correspond with the following sources:

- Foundries near the Chrysler Corporation and Plymouth Hamtramck Assembly Plants;
- Ford Motor Company, River Rouge Plant;
- Great Lakes Steel Division and other steel-making activities along the Detroit River; and
- McLouth Steel Corporation.

Brightness temperature plots over the latter three areas give maximum differences between the 3.8-μm and 11-μm data of 24.1 K, 26.0 K, and 26.2 K, respectively. Using the methods described in the previous section and by Dozier (1981), and assuming that a non-"hot" urban 3.8-μm pixel represents an appropriate "background" blackbody temperature (T_b), we can calculate the blackbody temperatures of the "hot" sources and the portions of the 1.1-km pixels covered by these sources. The results of these calculations are presented in Table 3. The high target blackbody temperatures (T_t) for these "hot" areas correspond well with steel producing activities, although the actual sources of the "hot" targets are difficult to ascertain using 1.1-km resolution data. The very small portion of the 1.1-km pixel filled by the "hot" target argues for targets on the order of 10^4 m^2. The high temperature areas shown in Figure 1 and tabulated in Table 2 are also associated with steel production.

Figure 8 is a 3.8-μm nighttime image of the Persian Gulf area. For comparison Figure 9 is a map of

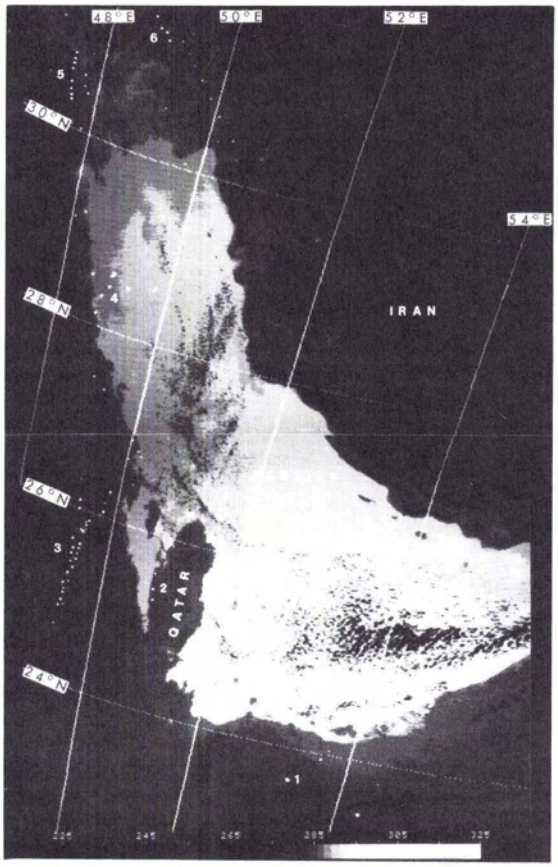

FIG. 8. NOAA-6 3.8-μm image of the Persian Gulf area taken on 4 March 1980 at 1523 GMT. The high temperature areas appear white and are waste gas flares from the oil wells in the region. The numbered flare areas correspond to the following oil fields (see Figure 9): (1) Bu Hasa, (2) Dukhan, (3) Ghawar, (4) Safoniya, (5) Rumaila, and (6) Marun. The black areas in the Persian Gulf are clouds.

TABLE 3. CALCULATION OF "HOT" TARGET TEMPERATURES AND PORTION OF 1.1-km PIXEL COVERED BY TARGET

Area	3.8 μm Brightness Temp. (T_3)	11 μm Brightness Temp.[1] (T_4)	"Background" Temp.[2] (T_b)	Calculated "Hot" Blackbody Target Temp. (T_t)	Calculated Portion of 1.1-km Pixel Covered by Target (P)	
2 Fig. 7b	310.3K	286.2K	284.0K	521.4K	0.0047	(5.2×10^3 m^2)
3 Fig. 7b	313.7K	287.7K	283.1K	463.1K	0.0144	(15.8×10^3 m^2)
4 Fig. 7b	312.5K	286.3K	282.7K	483.4K	0.0096	(10.6×10^3 m^2)
Gas flare Fig. 8	321.0K	280.0K	279.0K	790.2K	0.0007	(770 m^2)

[1] T_4 brightness temperatures have been corrected to compensate for atmospheric and water vapor effects in a manner similar to that used by McClain (1980).
[2] T_b is the brightness temperature of a non-"hot" 3.8-μm pixel.

FIG. 9. Map of the Middle East oil fields based on a CIA map entitled "Middle East Area Oilfields and Facilities." Heavily shaded areas represent oil fields.

the Middle East oil fields. The oil fields show up as "hot" spots because of waste gas flaring. Nighttime flaring has been documented by Croft (1978, 1979) using the low-light visible-band channel (0.4 to 1.1 μm) on board the spacecraft of the U.S. Air Force Defense Meteorological Satellite Program (DMSP). Croft (1979) points out, however, that these flare areas saturate the visible-band sensor and limit quantitative analyses. The NOAA-6 3.8-μm channel will saturate at a brightness temperature of 321 K. Many gas flares occupy only a very small portion of a 1.1-km pixel and, therefore, even at their high temperatures, do not cause the entire pixel to reach saturation brightness temperature. Some gas flare areas, however, do saturate the sensor. Such saturation, will be confined to individual pixels and will not affect adjacent pixels as it does in the visible-band DMSP data. A representative brightness temperature plot over one of the non-saturated flares gave a difference of 41 K between the 3.8-μm and 11-μm data. The "hot" blackbody target temperature was determined to be 790 K, and the area of the 1.1-km pixel covered by the target was 847 m^2 (see Table 3). This probably represents a composite of the bright, visible part of the flare and the invisible hot combustion products.

CONCLUSIONS

Although designed to complement the 11-μm thermal IR channel for sea surface temperature computations, the 3.8-μm channel is also useful for identifying subresolution scale high temperature sources. Because of reflected solar radiation contamination in the 3.8-μm channel, positive identification of such sources is only feasible at present with nighttime data. Employing the algorithm of Dozier (1981), it is possible to determine the blackbody temperature of these sources and the portions of the 1.1-km pixels covered by the "hot" targets. The present sensor saturation limit, however, restricts the range over which the technique can be applied. In spite of this drawback, joint use of the two thermal channels on board the current NOAA operational satellites raises some exciting

possibilities for remote sensing researchers. Beside the military applications of detecting steel and oil producing areas, other possible uses of the 3.8-μm data include studying volcanic areas, attempting to detect geothermal activity, discriminating active burning areas of forest fires, and navigational registration for the TIROS-N series latitude-longitude gridding calculations.

ACKNOWLEDGMENTS

The authors would like to thank Dr. Jim Gatlin of NASA Goddard Space Flight Center for his valuable assistance in processing the NOAA-6 data, Dr. E. Paul McClain and Dr. Warren Hovis for their thoughtful reviews of the manuscript, Scott Staggs for his annotation of the satellite imagery, and Mrs. Olivia Smith for her careful preparation of the manuscript. The paper was initiated and completed while one of the authors (J.D.) was supported by a Senior Postdoctoral Research Associateship from the National Research Council, National Academy of Sciences.

REFERENCES

Carlson, T. N., J. N. Augustine, and F. E. Boland, 1977. Potential Application of Satellite Temperature Measurements in the Analysis of Land Use over Urban Areas, *Bulletin of the American Meteorological Society*. 58, 1301-1303.

Croft, T. A., 1978. Nighttime Images of the Earth from Space. *Scientific American*, 239, 86-98.

———, 1979. *The Brightness of Lights on Earth at Night, Digitally Recorded by DMSP Satellite*. USGS PO57301, U.S. Geological Survey, Reston, Virginia.

Dozier, J., 1981. A Method for Satellite Identification of Surface Temperature Fields of Sub-Pixel Resolution. *Remote Sensing of Environment*, in press.

Kidwell, K. B., 1979. *NOAA Polar Orbiter Data (TIROS-N and NOAA-6) Users Guide*. NOAA Satellite Data Services Division, Washington, D.C.

Lloyd, J. M., 1975. *Thermal Imaging Systems*, Plenum Press, New York.

Matson, M., E. P. McClain, D. F. McGinnis, Jr., and J. A. Pritchard, 1978. Satellite Detection of Urban Heat Islands. *Monthly Weather Review*, 106, 1725-1734.

Matson, M., and R. V. Legeckis, 1980. Urban Heat Islands Detected by Satellite. *Bulletin of the American Meteorological Society*, 61, 212.

McClain, E. P., 1980. Multiple Atmospheric-Window Techniques for Satellite-Derived Sea Surface Temperatures. *COSPAR/SCOR/IUCRM Symposium on Oceanography from Space*, Venice, Italy, May 26-30, 1980.

Pease, R. W., C. B. Jenner, and J. E. Lewis, 1980. *The Influences of Land Use and Land Cover on Climate: An Analysis of the Washington-Baltimore Area that Couples Remote Sensing with Numerical Simulation*. U.S. Geological Survey Professional Paper 1099-A, U.S. Geological Survey, Washington, D.C.

Price, J. C., 1979. Assessment of the Urban Heat Island Effect through the Use of Satellite Data. *Monthly Weather Review*, 107, 1554-1557.

Schwalb, A., 1979. *The TIROS-N/NOAA A-G Satellite Series*. NOAA Technical Memorandum NESS 95, Washington, D.C.

Suits, G. H., 1975. The Nature of Electromagnetic Radiation. In *Manual of Remote Sensing*, R. G. Reeves, ed., American Society of Photogrammetry, Falls Church, Virginia, vol. 1, 51-73.

Weinreb, M. P., and M. L. Hill, 1980. *Calculation of Atmospheric Radiances and Brightness Temperatures in Infrared Window Channels of Satellite Radiometers*. NOAA Technical Report NESS 80, Washington, D.C.

(Received 22 August 1980; revised and accepted 21 March 1981)
